

Theoretical model for multi-orbital Kondo screening in strongly correlated molecules with several unpaired electrons

Aitor Calvo-Fernández,^{1,2,*} Manish Kumar,^{3,4,*} Diego Soler-Polo,³
Asier Eiguren,^{1,2,5} María Blanco-Rey,^{6,2,7,†} and Pavel Jelínek^{3,8,†}

¹*Departamento de Física, Universidad del País Vasco UPV-EHU, 48080 Leioa, Spain*

²*Donostia International Physics Center (DIPC), 20018 Donostia-San Sebastián, Spain*

³*Institute of Physics, Academy of Sciences of the Czech Republic,
Cukrovarnicka 10, Prague 6, CZ 16200, Czech Republic*

⁴*Department of Condensed Matter Physics, Faculty of Mathematics and Physics, Charles University, Prague, Czech Republic*

⁵*EHU Quantum Center, Universidad del País Vasco UPV-EHU, 48080 Leioa, Spain*

⁶*Departamento de Polímeros y Materiales Avanzados: Física, Química y Tecnología,
Universidad del País Vasco UPV-EHU, 20018 Donostia-San Sebastián, Spain*

⁷*Centro de Física de Materiales CFM/MPC (CSIC-UPV/EHU), 20018 Donostia-San Sebastián, Spain*

⁸*Regional Centre of Advanced Technologies and Materials,
Czech Advanced Technology and Research Institute (CATRIN),
Palacký University Olomouc, Olomouc 78371, Czech Republic*

(Dated: October 17, 2024)

The mechanism of Kondo screening in strongly correlated molecules with several unpaired electrons on a metal surface is still under debate. Here, we provide a theoretical framework that rationalizes the emergence of Kondo screening involving several extended molecular orbitals with unpaired electrons. We introduce a perturbative model, which provides simple rules to identify the presence of antiferromagnetic spin-flip channels involving charged molecular multiplets responsible for Kondo screening. The Kondo regime is confirmed by numerical renormalization group calculations. In addition, we introduce the concept of Kondo orbitals as molecular orbitals associated with the Kondo screening process, which provide a direct interpretation of experimental dI/dV maps of Kondo resonances. We demonstrate that this theoretical framework can be applied to different strongly correlated open-shell molecules on metal surfaces, obtaining good agreement with previously published experimental data.

I. INTRODUCTION

The Kondo effect [1, 2] is a widely studied many-body phenomenon in solid state physics, which has received a lot of attention. The origin of the Kondo effect is related to the exchange interaction between a single magnetic impurity and conduction electrons in a non-magnetic metal. This scattering process may establish a many-body singlet ground state, which is manifested as a strong zero-energy resonance in the spectral function. Originally, the Kondo effect was observed in transport measurements in non-magnetic metals with a diluted concentration of magnetic impurities [3, 4]. Later, it was also observed in single atoms with partially occupied d -electrons on metallic substrates by scanning tunneling microscopy [5–8]. More recently, it has been demonstrated that unpaired electrons in extended molecular orbitals (MO) can also act as magnetic impurities and scatter conduction electrons from the underlying metal surface, leading to the molecular Kondo effect [9–27].

While the conventional $S = 1/2$ Kondo effect for magnetic impurities has been extensively studied and is very well understood, the mechanism of the Kondo effect in magnetic impurities with various strongly corre-

lated unpaired electrons is barely explored. In particular, here the so-called underscreened Kondo effect can take place if there are less than $2S$ screening channels [28], whereby the ground state shows a residual magnetic moment. This effect was extensively studied for quantum dot systems both experimentally [29, 30] and theoretically [31, 32]. Recently, the Kondo effect in molecular systems with several unpaired electrons was reported for open-shell triplet ($S = 1$) nanographenes [24, 27] and porphyrins [33–35] on metallic surfaces. The former case was theoretically rationalized within the one-crossing approximation [26].

Nevertheless, a broader picture of the Kondo effect in open-shell molecular systems with several unpaired electrons is still missing. This is a multi-orbital Kondo problem where the involved orbitals have an extended non-trivial spatial distribution. Therefore, in order to describe it we need to consider, on the same footing, aspects such as the number and symmetry of the screening channels defined by the MOs hosting the unpaired electrons, as well as the strongly correlated multiplet (i.e., many-electron) nature of the molecular electronic configuration, which cannot be properly described by mean-field theories such as density functional theory (DFT).

In this work, we present a theoretical framework for the molecular multi-orbital Kondo effect and apply it to strongly correlated molecules deposited on metal surfaces. The theoretical framework consists of three steps:

* These authors contributed equally to this work.

† Corresponding author

(i) Complete Active Space Configuration Interaction (CASCI) calculations [36] accurately provide the electronic states of neutral and charged molecular multiplets; (ii) a generalized perturbative analysis of the Anderson Hamiltonian, which accounts for the multiplet structure, reveals the antiferromagnetically coupled channels responsible for Kondo screening by the metal substrate; and finally (iii) numerical renormalization group (NRG) calculations [37] provide observable quantities. In addition, we introduce the concept of *Kondo orbitals* (KO) as unitary transformations of the MOs inside the active space that show pure antiferromagnetic or ferromagnetic coupling to conduction electrons. Upon critical comparison with the well-established quantum-chemical concept of natural transition orbitals (NTO), we show that the KOs can be directly compared to experimental dI/dV maps of the Kondo signal.

To benchmark the proposed theoretical framework, we select examples of open-shell molecules with several unpaired spins deposited on Au(111) surfaces, where Kondo resonances were experimentally observed. In particular, we try to reproduce Kondo features observed in extended porphyrins [35] and graphene nano-sized flakes [24, 38, 39]. By the combination of the Ovchinnikov rules [40], charge transfer to the substrate, and *ad hoc* radical formation by partial dehydrogenation of edge carbon sites using STM manipulation, high-spin states can be realized in these systems, resulting in the presence of coexisting underscreened Kondo and spin excitation features in the dI/dV signals [41].

II. RATIONALIZATION OF THE KONDO PEAK

A. Multi-channel Anderson model

To model a molecule adsorbed on a metallic surface we use the ionic Anderson impurity model [42, 43] given by the Hamiltonian

$$\hat{\mathcal{H}}_A = \hat{H}_{\text{mol}} + \hat{H}_{\text{con}} + \hat{H}_{\text{hyb}}. \quad (1)$$

The molecular part of the Hamiltonian is given by the term

$$\hat{H}_{\text{mol}} = \sum_{M,m} \epsilon_M |Mm\rangle \langle Mm|, \quad (2)$$

which contains the energies ϵ_M of the multiplet states $|Mm\rangle$ obtained from CASCI calculations, which will be described in Section III. Here M denotes the order of the multiplet state and m is the magnetic quantum number. Since we are mainly interested in capturing the Kondo physics of the system, we keep only the neutral N_0 -particle ground multiplet and charged multiplets with $N_0 \pm 1$ particles involved in virtual spin excitations, as discussed later. We incorporate the effect of the substrate on the molecule by shifting the charged multiplet energies as $\epsilon_M = E_M + (N_M - N_0)\mu$, where N_M is the

number of particles in the multiplet M , E_M is the energy of the multiplet in gas phase, and μ is the chemical potential induced by the substrate.

The substrate conduction electrons are described by the term

$$\hat{H}_{\text{con}} = \sum_{\alpha,\sigma} \int_{-D}^D d\epsilon \hat{c}_{\epsilon\alpha\sigma}^\dagger \hat{c}_{\epsilon\alpha\sigma} \epsilon, \quad (3)$$

where $\hat{c}_{\epsilon\alpha\sigma}^\dagger$ ($\hat{c}_{\epsilon\alpha\sigma}$) creates (annihilates) a conduction electron with spin σ and energy ϵ covering a band-width from $-D$ to D , belonging to channel α . The electronic states in channel α couple to a single one-electron MO, which can be labeled the same as α , and are constructed as

$$|\epsilon\alpha\sigma\rangle = \frac{1}{[\rho_\alpha(\epsilon)]^{\frac{1}{2}} V_\alpha(\epsilon)} \sum_{\mathbf{k}} V_{\alpha\mathbf{k}} |\mathbf{k}\sigma\rangle \delta(\epsilon - \epsilon_{\mathbf{k}}), \quad (4)$$

where $V_{\alpha\mathbf{k}}$ is the tunneling amplitude for an electron in MO α into a conduction state with momentum \mathbf{k} , and $[\rho_\alpha(\epsilon)]^{\frac{1}{2}} V_\alpha(\epsilon)$ is the integrated tunneling amplitude between electrons in the MO and channel with the same label α , given by $\rho_\alpha(\epsilon) V_\alpha^2(\epsilon) = \sum_{\mathbf{k}} |V_{\alpha\mathbf{k}}|^2 \delta(\epsilon - \epsilon_{\mathbf{k}})$. The integrated tunneling amplitude contains the density of states $\rho_\alpha(\epsilon)$ and the tunneling amplitude $V_\alpha(\epsilon)$ in the channel representation. We take the usual wide-band limit where the hybridization is energy independent in the bandwidth of interest and also equal for all MOs, i.e. $[\rho_\alpha(\epsilon)]^{\frac{1}{2}} V_\alpha(\epsilon) = \rho^{\frac{1}{2}} V$. We assume the constant coupling approximation to all MOs, as they consist of π -orbitals. Moreover, molecules considered here are planar molecules physisorbed on a metal surface. Thus, MOs have a very similar electronic overlap with the substrate, and the constant coupling approximation seems to be justified.

The coupling of the molecule to the substrate is described by the hybridization term

$$\begin{aligned} \hat{H}_{\text{hyb}} = & \sum_{M_i m_i} \sum_{M_f m_f} \sum_{\alpha\sigma} \int_{-D}^D d\epsilon \rho^{\frac{1}{2}} V \\ & \times \langle M_f m_f | \hat{f}_{\alpha\sigma}^\dagger | M_i m_i \rangle | M_f m_f \rangle \langle M_i m_i | \hat{c}_{\epsilon\alpha\sigma} + \text{h.c.}, \end{aligned} \quad (5)$$

which introduces processes where the impurity gains (loses) an electron in MO α with spin σ , which is created (annihilated) by the operator $\hat{f}_{\alpha\sigma}^\dagger$ ($\hat{f}_{\alpha\sigma}$), and goes from the initial state $|M_i m_i\rangle$ to the final state $|M_f m_f\rangle$.

B. Effective Kondo model

At energy scales much smaller than the molecular excitation energies, the charged multiplets can be integrated out using the Schrieffer-Wolff transformation [44]. This transformation can be generalized to ionic and multi-channel Kondo systems [31, 45, 46]. We perform the transformation to second order in perturbation theory by summing over the virtual processes depicted in Fig. 1, which involve virtual fluctuations of the molecule into

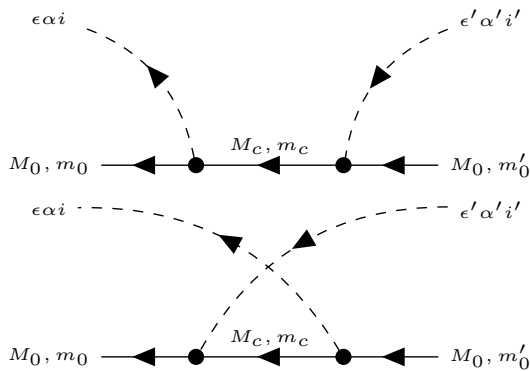


FIG. 1. Feynman diagrams for virtual scattering process through the intermediate molecular multiplet M_c with occupation $N_0 + 1$ (top) and $N_0 - 1$ (bottom).

the charged multiplets (see Appendix A). The resulting effective interaction, ignoring the potential term, is given

$$C(M_c)_{\alpha\alpha'} = \begin{cases} \frac{\langle M_c || \hat{f}_\alpha^\dagger || M_0 \rangle^* \langle M_c || \hat{f}_{\alpha'}^\dagger || M_0 \rangle}{(S_0 + \frac{1}{2})}, & \text{if } N_c = N_0 + 1, S_c = S_0 - \frac{1}{2}, \\ \frac{\langle M_0 || \hat{f}_{\alpha'}^\dagger || M_c \rangle \langle M_0 || \hat{f}_\alpha^\dagger || M_c \rangle^*}{S_0}, & \text{if } N_c = N_0 - 1, S_c = S_0 - \frac{1}{2}, \\ -\frac{\langle M_c || \hat{f}_\alpha^\dagger || M_0 \rangle^* \langle M_c || \hat{f}_{\alpha'}^\dagger || M_0 \rangle}{(S_0 + \frac{1}{2})}, & \text{if } N_c = N_0 + 1, S_c = S_0 + \frac{1}{2}, \\ -\frac{\langle M_0 || \hat{f}_{\alpha'}^\dagger || M_c \rangle \langle M_0 || \hat{f}_\alpha^\dagger || M_c \rangle^*}{(S_0 + 1)}, & \text{if } N_c = N_0 - 1, S_c = S_0 + \frac{1}{2}, \end{cases} \quad (8)$$

where $\langle \dots || \hat{f}_\alpha^\dagger || \dots \rangle$ are reduced matrix elements of the creation operator and N_0 (N_c) and S_0 (S_c) are the occupation and spin of the ground (excited) multiplet, respectively.

C. Kondo orbitals

Using the information contained in the coupling constants $J_{\alpha\alpha'}$ characterizing the scattering between *channels*, we can identify the *orbitals* involved in the screening of the molecular spin through the virtual processes depicted in Fig. 1. The poor man's scaling [42] equation for the coupling constant matrix, given to second order in perturbation theory, is

$$\delta J = \rho J^2 \frac{|\delta D|}{D}, \quad (9)$$

which is an extension of the familiar scaling of the magnetic coupling constant to a matrix form (see Appendix B). In general, the scaling of each specific term $J_{\alpha\alpha'}$ depends quadratically on the values of other matrix elements, which hinders the solution of the equation and therefore the identification of the channels as ferromag-

by the Kondo Hamiltonian

$$\hat{H}_K = \sum_{\alpha\alpha'} J_{\alpha\alpha'} \hat{\mathbf{S}} \cdot \hat{\mathbf{s}}_{\alpha\alpha'}, \quad (6)$$

where J is the matrix containing the effective coupling constants $J_{\alpha\alpha'}$, $\hat{\mathbf{S}}$ is the molecular spin operator, and $\hat{\mathbf{s}}_{\alpha\alpha'} = \sum_{ii'} \frac{1}{2} \psi_{\alpha i}^\dagger \vec{\sigma}_{ii'} \psi_{\alpha' i'}$ is the local spin density operator [31]. In this Hamiltonian, the molecule is reduced to the spin degree of freedom of the ground multiplet. The conduction electrons scatter off this spin by interchanging spin, $i' \rightarrow i$, and hopping between channels, $\alpha' \rightarrow \alpha$. The strength of the coupling between channels is given by the constants

$$J_{\alpha\alpha'} = V^2 \sum_{M_c} \frac{C(M_c)_{\alpha\alpha'}}{\epsilon_{M_c} - \epsilon_{M_0}}, \quad (7)$$

which contain contributions from all the excited multiplets M_c weighted by their excitation energy and a coefficient $C(M)_{\alpha\alpha'}$ determined by the many-body structure of the multiplets (see Appendix A and E),

netic (FM) or antiferromagnetic (AFM). To circumvent this difficulty, we diagonalize the hermitian matrix J to rewrite the effective interaction as $H_K = \sum_a j_a \hat{\mathbf{S}} \cdot \hat{\mathbf{s}}_{aa}$, where j_a are the eigenvalues and $|a\rangle = \sum_\alpha U_{\alpha a} |\alpha\rangle$ the corresponding rotated MOs, which we denote *Kondo orbitals* (KO) in the following.

In the KO basis, the scaling equations become decoupled and we can conclude that for $j_a > 0$ the coupling is AFM and will increase as the energy scale is lowered, while for $j_a < 0$ it is FM and will decrease with the lowering of the energy scale. Thus, the $2S_0$ AFM channels with the largest j_a will screen the impurity spin, while the other AFM channels (if any) and the FM channels will decouple at low temperatures. Hence, we expect the KOs coupled to the screening AFM channels to host spectral peaks at sufficiently low temperatures, which allows us to predict the experimental dI/dV maps to match the spatial distribution of those KOs.

D. NRG and spectral functions

We use the NRG method as implemented in the `PointGroupNRG` code [47, 48] to solve the Ander-

son Hamiltonian for each molecule and compute zero-temperature orbital-resolved spectral functions that we can compare with experiment. We work in the KO basis, which allows us to leverage the Kondo orbital analysis by identifying the channels with the smallest contribution to the Kondo screening and discard them to keep a maximum of two, thereby making the systems tractable with the NRG.

Following the previous scaling arguments, the AFM channels with largest j_a should have the largest Kondo temperature and hence the largest half-width at half-maximum (HWHM) in the spectral peaks. To prove the validity of our model, we show that our free parameters $\Gamma = \rho\pi V^2$ and μ can be adjusted to match the experimental observations: we require the zero-bias peaks of each KO to have the appropriate full-width at half-maximum $\text{FWHM} = 2 \cdot \text{HWHM}$, which we estimate by subtracting the contribution from the temperature T_{ex} [49],

$$\text{FWHM}_{\text{NRG}} = \sqrt{\text{FWHM}_{\text{ex}}^2 - (2\pi k_B T_{\text{ex}})^2}, \quad (10)$$

where FWHM_{NRG} is the calculated value and FWHM_{ex} is the experimental value, usually obtained by fitting line-shapes to the dI/dV data. In the cases where an under-screened ground state is observed, we also require the rest of the zero-bias peaks to have a HWHM_{NRG} lower than the experimental temperature. For comparison with experiment, we have to take into account that the measurements are made at a non-zero temperature, causing the peaks to progressively flatten as their associated HWHM goes past the Kondo temperature [50], which we take to be equal to the zero-temperature half-width obtained via NRG, $T_K = \text{HWHM}_{\text{NRG}}$. This is an effect that we cannot reproduce in our calculations.

We choose the half-bandwidth $D = 10\text{eV}$ value for all systems, which is larger than all excitation energies, as we have found this to yield smoother peaks with heights closer to $1/(\pi\Gamma)$. We use a discretization parameter $\Lambda = 2$ and we keep 3000 multiplets at each NRG step. To obtain smoother spectral curves, we average the results over two interleaved discretization grids with twisting parameters $z = 0.0$ and 0.5 [51].

III. ELECTRONIC STRUCTURE

We have characterized the electronic structures of the studied molecules by means of DFT + CASCI calculations. We optimized the geometries at the PBE0 level of theory [52] with the DFT code FHI-aims [53]. With this optimized geometry, we perform an *ab initio* CASCI calculation starting from the restricted DFT with the PBE functional [54] from which we obtain the many-body multiplets, their energies, the natural orbitals and their occupations [55]. We perform the latter calculation with the quantum chemistry code ORCA [56, 57] in order to construct the integrals that define the molecular Hamil-

tonian in the basis of MOs around Fermi energy:

$$t_{ij} = \int \phi_i(\mathbf{r}) \left(-\frac{\hbar}{2m} \nabla^2 + V(\mathbf{r}) \right) \phi_j(\mathbf{r}) d^3\mathbf{r} \quad (11)$$

and

$$\mathcal{V}_{ijkl} = \frac{1}{4\pi\epsilon_0} \int \frac{\phi_i(\mathbf{r})\phi_j(\mathbf{r}')\phi_k(\mathbf{r}')\phi_l(\mathbf{r})}{|\mathbf{r}-\mathbf{r}'|} d^3\mathbf{r}d^3\mathbf{r}', \quad (12)$$

where the indices i, j, k, l label molecular orbitals, ranging over the set of such orbitals selected as the active space. The one-electron potential $V(\mathbf{r})$ in Eq. 11 includes the potentials of the ions and the potential from the electrons in the occupied inactive orbitals, that is,

$$V(\mathbf{r}) = \frac{1}{4\pi\epsilon_0} \sum_{\gamma} \frac{eZ_{\gamma}}{|\mathbf{R}_{\gamma}-\mathbf{r}|} + \sum_{\lambda} \int \frac{|\phi_{\lambda}(\mathbf{r}')|^2}{|\mathbf{r}-\mathbf{r}'|} d^3\mathbf{r},$$

where γ runs over the nuclei, Z_{γ} is the charge of the nuclei and the index λ runs over occupied inactive molecular orbitals given by $\phi_{\lambda}(\mathbf{r})$, which are always doubly-occupied in the possible Slater determinants of our calculation. We then build up the many-body *ab initio* molecular Hamiltonian $\hat{\mathcal{H}}_{\text{CAS}}$ with those coefficients:

$$\hat{\mathcal{H}}_{\text{CAS}} = \sum_{i,j,\sigma} t_{ij} \hat{C}_{i\sigma}^{\dagger} \hat{C}_{j\sigma} + \sum_{i,j,k,l,\sigma,\sigma'} \mathcal{V}_{ijkl} \hat{C}_{i\sigma}^{\dagger} \hat{C}_{j\sigma'}^{\dagger} \hat{C}_{k\sigma'} \hat{C}_{l\sigma}. \quad (13)$$

This many-body Hamiltonian in Eq. 13 can finally be cast into a matrix and solved by exact diagonalization in a selected active space. The active space is composed by selected frontier DFT orbitals around the Fermi level (see Section IV), which capture the relevant electronic configurations contributing to the ground state and low-energy excited states. The expansion in Slater determinants, which represents the many-body multiplets, is employed to analyze the presence of Kondo screening processes as well as for the NRG calculation. These multiplets for the neutral and charged molecules studied in section IV are presented in the Appendix D.

IV. RESULTS

In this section, we apply the proposed theoretical model to rationalize previous experimental data reporting the Kondo effect in molecules with several unpaired electrons on the metallic surface. For each system, we provide the calculated CASCI orbitals and the electronic configuration of the ground multiplet. We also give the calculated j_a coupling constants as a function of μ and, for the chosen μ value, the KOs together with their dI/dV maps. The NTOs and KOs are linear combinations of the orbitals of the active space for the CASCI calculation, and therefore can be expanded in the basis of atomic orbitals. Using this atomic orbital basis, we simulated the dI/dV maps of NTOs and KOs presented in the manuscript by applying the PP-STM code [58],

which takes into account the selection rules of the tunneling processes between tip and molecule. When using the NTOs, each eigenvalue of the transition density matrix provides the relative weight of a particular transition to the dI/dV map. This analysis is then compared with experimental results using spectral functions calculated with the NRG for a value of the hybridization Γ .

A. Zinc porphyrin (**PorA₂**)

First we discuss a porphyrin molecule with extended π -system **PorA₂**, synthesised and studied in Ref. [35]. It hosts two radical centers at opposite pyrrol sites, created by C-H bond breaking with STM manipulation. Its open-shell configuration is 0.46 eV more stable than the closed-shell one and the ground state is a triplet $S = 1$. The dI/dV spectroscopy obtained at $T_{\text{ex}} = 4.5 \text{ K} \approx 0.39 \text{ meV}$ shows steps associated to inelastic spin excitation at $\pm 22 \text{ mV}$ and a zero-bias feature, interpreted as a Kondo resonance.

In Fig. 2 we show the main MOs obtained by DFT and the main Slater determinants that make up the ground state of the molecule in gas phase. Applying the Kondo orbital analysis from Sections IIB and IIC, we find two main AFM channels in the allowed μ range, as shown in Fig. 3 a). We choose $\mu = 3 \text{ eV}$, for which we compute the associated KOs shown in Fig. 3 c,d), which correspond very well with the HOMO and LUMO orbitals, respectively. Their dI/dV maps, shown in Fig. 3 e,f), are compatible with the measured STM maps shown in Fig. 3 g), so that the two channels coupled to the KOs can participate in the screening. The calculated spectral functions are shown in Fig. 3 b). They feature zero-bias peaks with $\text{HWHM}_{\text{NRG}} = 0.8 \text{ meV}$ and 0.5 meV for a hybridization $\Gamma = 0.8 \text{ eV}$. In Ref. [35] the authors use Ternes' model [41] to fit the dI/dV spectrum with an AFM coupling of $|\rho J| = 0.14$. We obtain an equivalent coupling $\rho j_1 \approx \rho j_2 \approx 0.14$ using $\Gamma = 0.55 \text{ eV}$, but this results in $T_{\text{K}} = \text{HWHM}_{\text{NRG}} \approx 0.8 \text{ K}$ and 0.5 K for KOs 1 and 2, respectively, both below the experimental temperature. Note, however, that in the fitting used in Ref. [35] the spin-excitation cusps are considered as well as

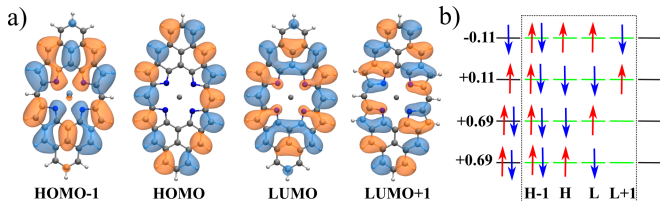


FIG. 2. a) The four main DFT orbitals employed in the active space calculation for the **PorA₂** molecule. b) Major Slater determinants for the ground states **PorA₂**. The dashed box contains the four frontier orbitals: HOMO-1, HOMO, LUMO, and LUMO+1. The values are the coefficients of those determinants in the orbital wave function.

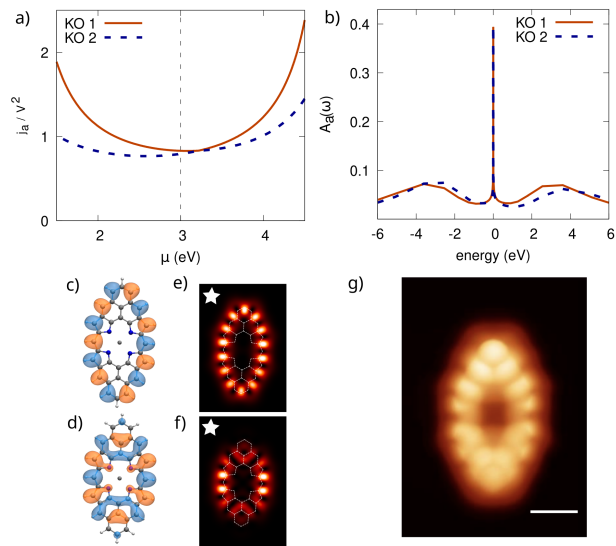


FIG. 3. Kondo screening results for **PorA₂**. (a) Rescaled coupling constants j_a/V^2 as a function of the chemical potential μ . The vertical dashed line indicates the value $\mu = 3 \text{ eV}$ used in the KO and NRG calculations. b) Zero-temperature spectral functions $A_a(\omega)$ obtained with NRG with the hybridization set to $\Gamma = 0.8 \text{ eV}$, yielding HWHM (T_{K}) values of 0.8 meV (9.3 K) and 0.5 meV (5.8 K) for the KOs 1 and 2, respectively. Orbital shapes for KOs c) 1 and d) 2, and e,f) their respective dI/dV maps. dI/dV maps of KOs with $T_{\text{K}} > T_{\text{ex}}$ are indicated with white stars. g) Experimental low-bias constant current STM image acquired at 5 meV adopted from Ref. [35].

the zero-bias peak.

B. Fused Aza-[3]-Triangulene ($4''^+$)

The spin S of $[N]$ -Triangulene increases linearly with the number N of units on the sides of the molecule according to Ovchinnikov's rule [40]. The value of S is decreased by $1/2$ when a N atom substitution is introduced at the center (Aza- $[N]$ -Triangulene). Further alterations of the spin state can be achieved by charge transfer upon adsorption on a metal, dehydrogenation, and also by fusing Triangulenes at different C sites. In Ref. [38] the fused Aza-[3]-Triangulene is reported. This molecule has open-shell character, with a $S = 1$ ground state and $+1$ net charge when adsorbed on Au(111). The conductance spectrum shows a zero-bias peak consistent with a Kondo effect at $T_{\text{ex}} = 4.3 \text{ K} \approx 0.37 \text{ meV}$. A fit to the Frota function [59] yields $\text{FWHM}_{\text{ex}} = 15.0 \text{ meV}$.

Our analysis shows that the KOs for this system are mostly combinations of the HOMO and LUMO orbitals, given in Fig. 4, across the whole μ range. For our calculations we use $\mu = 5 \text{ eV}$, which gives us similar coupling constants for the two KOs located in the lower (KO 1) and upper (KO 2) triangulenes, see Fig. 5 a,c-f). With this choice of μ , we expect STM signals in the lower

and upper triangulenes, in accordance with the experimental measurements shown in Fig. 5 g). In particular, we accurately reproduce the brighter sections in the lower part of the lower triangulene and in the outside left edge of the upper triangulene. The computed spectral functions, shown in Fig. 5 b), feature Kondo peaks with $\text{FWHM}_{\text{NRG}} = 14.6 \text{ meV}$ and 13.4 meV close to the temperature-corrected experimental value 14.8 meV for $\Gamma = 1.6 \text{ eV}$. The corresponding Kondo temperatures are $T_K = 84.7 \text{ K}$ and 77.8 K , well above the experimental temperature.

C. Rocket-shaped extended triangulene (ETRI)

The **ETRI** molecule is a graphene nanoribbon studied experimentally in Ref. [60]. Upon removal of two H atoms by STM tip, it acquires a $S = 1$ state. Here an underscreened Kondo effect is probed by Zeeman splitting of the zero-bias peak under the Kondo temperature, which is estimated to be $T_K \approx 6 \text{ K}$ from a Frota fitting of the dI/dV spectra, which has peak width of $\text{HWHM}_{\text{ex}} \approx 0.75 \text{ meV}$ measured at $T_{\text{ex}} = 1.3 \text{ K} \approx 0.11 \text{ meV}$.

To reproduce the experimental results, we chose a chemical potential $\mu = 4 \text{ meV}$ that gives us a stronger AFM coupling for the HOMO-shaped KO 1 located primarily in the lower half of the molecule, where the zero-bias peaks are most intense, see Fig. 6 and Fig. 7 a-e). Moreover, that value of μ is large enough to produce a sufficient separation in the coupling strengths of both KOs, so that for $\Gamma = 0.53 \text{ meV}$ the KO 1 has an associated $\text{HWHM}_{\text{NRG}} = 0.64 \text{ meV}$ ($T_K = 7.4 \text{ K} > T_{\text{ex}}$), close to the temperature-corrected experimental value 0.67 meV , while the KO 2 has $T_K = 0.08 \text{ K} \ll T_{\text{ex}}$ and thus we expect no Kondo signal from it. With these parameters we obtain the experimentally observed underscreened ground state as a result of an uneven magnetic coupling favoring the HOMO-like KO, which gives us the dI/dV map in Fig. 7 e). Here direct comparison between theory and experiment is not straightforward as the experimental STM image, shown in Fig. 7 g), was taken in a close tip-sample distance, where lateral relaxation of CO-tip substantially modifies the contrast [58]. Nevertheless, we still can find some similarities in the spatial distribution with predominant Kondo signal in lower part of the molecule.

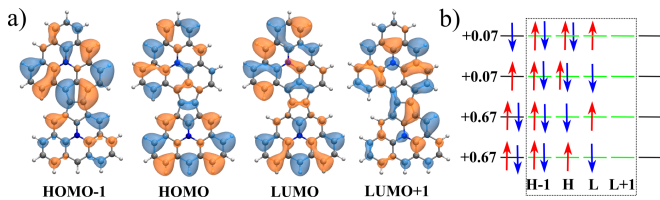


FIG. 4. Same information as in Fig. 2 for the $4''^+$ molecule.

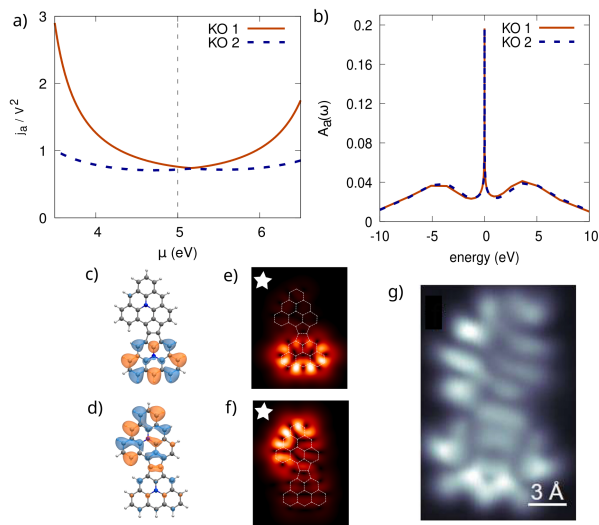


FIG. 5. Same information as in Fig. 3 for the $4''^+$ molecule with parameters $\mu = 5 \text{ eV}$ and $\Gamma = 1.6 \text{ eV}$, and spectral functions with FWHM (T_K) values 14.6 meV (84.7 K) and 13.4 meV (77.8 K) for KOs 1 and 2, respectively. The experimental constant current STM image acquired at 5 meV adopted from Ref. [38].

D. Aza-[5]-Triangulene (A5T)

The molecule **A5T** is experimentally studied in Ref. [39]. It has $S = 3/2$ in the neutral state, but due to charge transfer of an electron to the Au(111) substrate it shows a $S = 2$ ground state. Based on the splitting of the Kondo peaks upon the application of a magnetic field and the dI/dV maps, the authors conclude that this spin is partially screened at $T_{\text{ex}} = 1.2 \text{ K} \approx 0.1 \text{ meV}$ by a single channel associated with one of the molecular orbitals. The maximum Kondo temperature estimated from fits to a Frota function is $T_K = 11 \text{ K} \approx 0.9 \text{ meV}$ and the average is $9 \text{ K} \approx 0.8 \text{ meV}$.

DFT calculations for this molecule give us four degenerate molecular orbitals, shown in Fig. 8. For low values of μ , we find that the strongest KO has the shape of the HOMO-1, which is identified in Ref. [39] as the orbital responsible for the screening, while the second strongest KO resembles the HOMO, which would produce a dI/dV signal not observed in experiment, see Fig. 9 a,c-g). We choose $\mu = 4.3 \text{ eV}$ to obtain a sufficient separation between j_1 and j_2 and we fix $\Gamma = 1.42 \text{ eV}$, which gives us

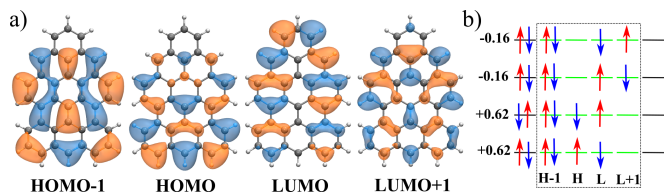


FIG. 6. Same information as in Fig. 2 for the **ETRI** molecule.

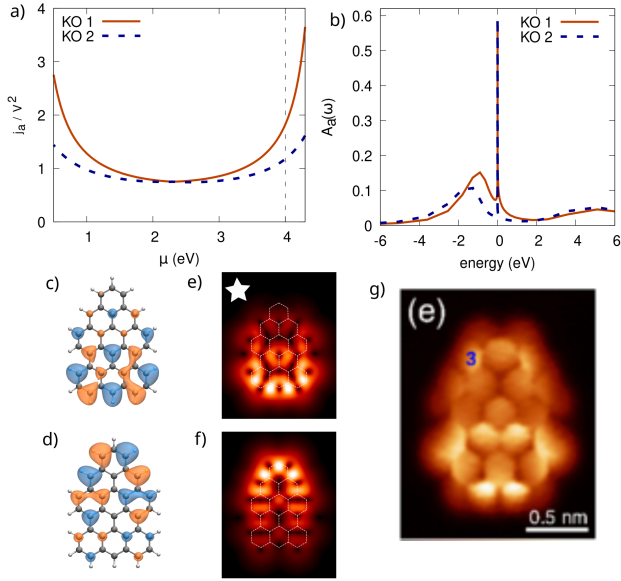


FIG. 7. Same information as in Fig. 3 for **ETRI** with parameters $\mu = 4$ eV and $\Gamma = 0.53$ eV, and spectral functions with HWHM (T_K) values 0.64 meV (7.4 K) and 0.007 meV (0.08 K) for KOs 1 and 2, respectively. The experimental constant current bond-resolved STM image acquired at 2 meV adopted from Ref. [60].

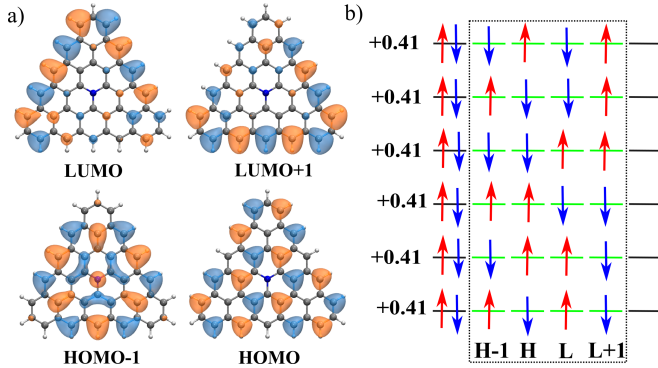


FIG. 8. Same information as in Fig. 2 for **A5T**.

for KO 1 $\text{HWHM}_{\text{NRG}} = 0.75$ meV ($T_K = 8.7$ K $> T_{\text{ex}}$), close to the temperature-corrected experimental value 0.74 meV, and for KO 2 $T_K = 0.7$ K $< T_{\text{ex}}$, corresponding to a one-channel underscreened impurity spin with the predicted dI/dV signal given in Fig. 9 e), which matches well with experimental dI/dV maps at 5 meV shown in Fig. 9g).

V. COMPARISON WITH NATURAL TRANSITION ORBITALS

The characteristic second-order processes leading to the effective magnetic interaction between the molecule and the substrate involve electron scattering processes where the impurity spin orientation changes from m_0 to

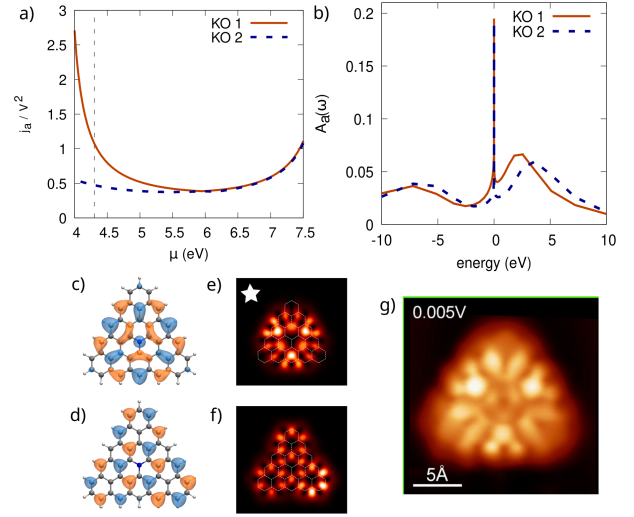


FIG. 9. Same information as in Fig. 5 for **A5T** with parameters $\mu = 4.3$ eV and $\Gamma = 1.42$ eV, with HWHM (T_K) values 0.75 meV (8.7 K) and 0.06 meV (0.7 K) for KOs 1 and 2, respectively. Only the KOs with the strongest AFM coupling are shown. Experimental dI/dV map taken at 5 meV adopted from Ref. [39].

$m_0 \pm 1$. This motivates invoking the NTOs [55] as the mediators of the spin-flip processes.

In their general definition, the NTOs are defined as the eigenvectors of the matrices $A = TT^\dagger$ and $B = T^\dagger T$, with the transition matrix elements of T defined in our case as

$$T_{\alpha\alpha'} = \langle M_0, m_0 - 1 | f_{\alpha\downarrow}^\dagger f_{\alpha'\uparrow} | M_0, m_0 \rangle \quad (14)$$

for a fixed m_0 in the range $-S_0 < m_0 \leq S_0$. For our spin-flip transitions, it can straightforwardly be shown that $T = T^\dagger$ and, consequently, $A = B$ (see Appendix C). Therefore, we obtain a single set of NTOs $|n\rangle$ with eigenvalues λ_n fulfilling $1 \geq \lambda_n \geq 0$. From these NTOs we can compute the spin-flip dI/dV map by summing the intensities obtained from each NTO weighted by their eigenvalues λ_n .

In Fig. 10 we compare the results of the KO+NRG analysis in Section IV with the dI/dV maps calculated from the NTO for **PorA₂** and **ETRI**. For **PorA₂**, KOs and NTOs are very similar and have the form of the HOMO and LUMO. The dI/dV maps obtained using both methods contain contributions from both MOs, resulting in intensity distributions that qualitatively match the experimental results. For **ETRI**, on the other hand, NTOs have similar weights for both MOs, resulting in a dI/dV map that extends across the entire molecule. This does not match the uneven underscreened ground state and neither the uneven spatial distribution observed in the experiment, which are well captured in the KO+NRG results. As in the case of **ETRI**, **A5T** (Fig. 9) also shows a discrepancy between the two approaches. In this case, we obtain four degenerate NTOs that combine with equal

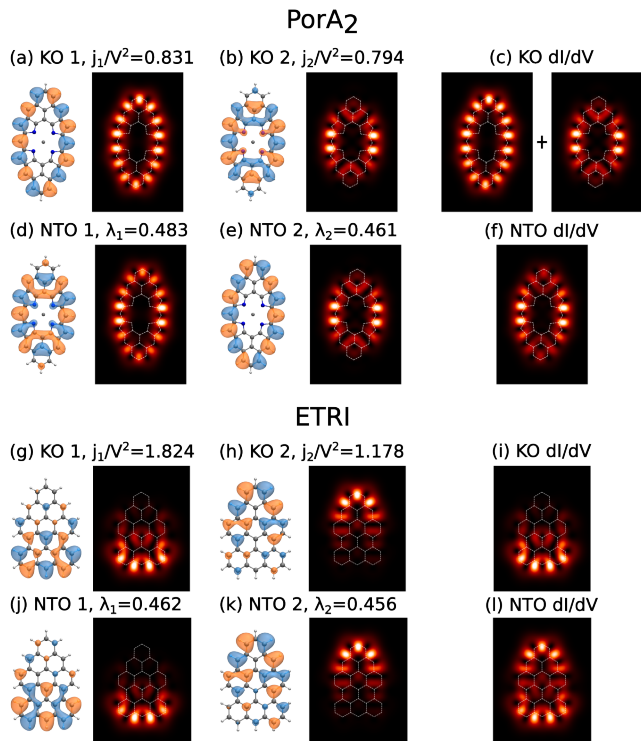


FIG. 10. Comparison of KOs and NTOs for **PorA₂** and **ETRI**. For **PorA₂** [**ETRI**] we show a,b) [g,h)] the KOs with the value of their rescaled couplings j_a/V^2 and their dI/dV map, c) [i)] the dI/dV map expected from the Kondo orbital analysis, d,e) [j,k)] the NTOs with their λ_a eigenvalue and their dI/dV maps, and f) [l)] the sum of the NTO dI/dV maps weighted by their eigenvalues.

weights to yield a dI/dV map that does not match the experiment.

The reason for the discrepancies between the NTO and KO+NRG Kondo maps is that the NTOs only take into account the composition of the ground state, leaving aside all the structure of excited states that is incorporated into the KO analysis through the Schrieffer-Wolff transformation and naturally into the NRG. This can be clearly seen by manipulating Eq. 14 to rewrite the matrix elements of T as

$$T_{\alpha\alpha'} = \frac{S_{m_0-1,m_0}^-}{4} \sum_{M_c} C(M_c)_{\alpha\alpha'}. \quad (15)$$

where S_{m_0-1,m_0}^- is the matrix element of the spin lowering operator and $C(M_c)_{\alpha\alpha'}$ are the same coefficients appearing in Eq. 7 and given by Eq. 8 (see Appendix C). The only difference between T and J , apart from a constant factor, is the energy denominator in J that acts as a weight in the sum of the contributions. Thus, we expect T to retain the features of J inasmuch as the excitation energies of the excited multiplets M_c with sizeable Lehmann amplitudes are similar (see Appendix E). When this condition is met, T can be regarded as an ap-

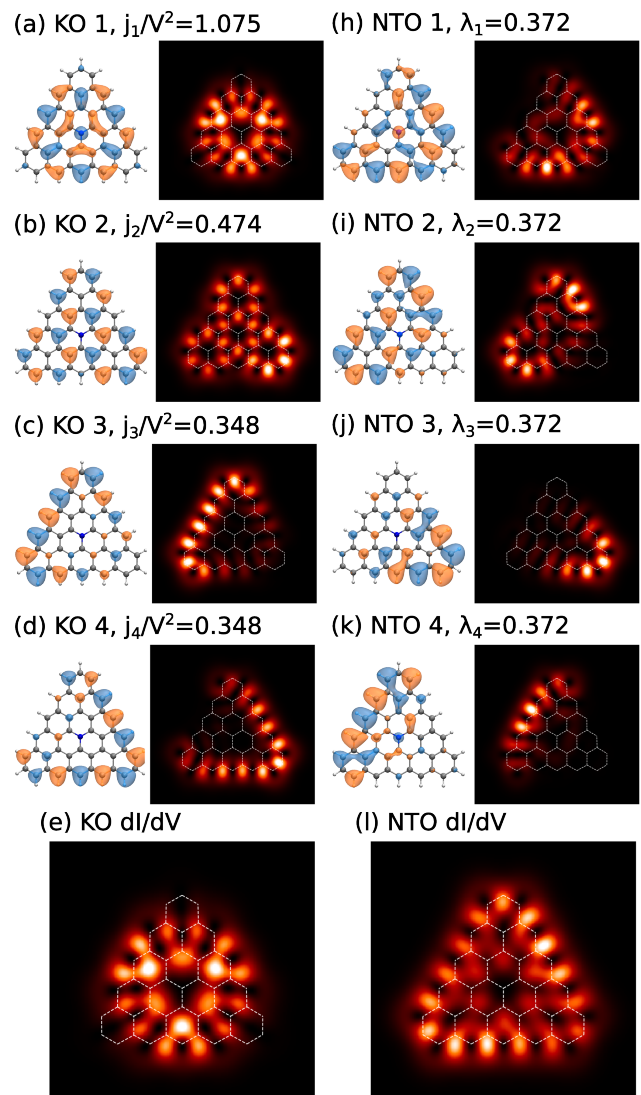


FIG. 11. Comparison of KOs and NTOs for **A5T**. a-d) KOs with their j_a/V^2 values and dI/dV maps, e) dI/dV map expected from the Kondo orbital analysis, h-k) NTOs with their λ_a eigenvalues and dI/dV maps, and l) sum of the NTO dI/dV maps weighted by their eigenvalues.

proximation of J and the signs of its eigenvalues tell us whether each associated NTO mediates a FM or AFM interaction (the eigenstates of T are the same as those of T^2 with signs $\pm\sqrt{\lambda_n}$).

VI. CONCLUSIONS

We presented the perturbative approach of spin-flip processes between various molecular multiplets, which enables us to identify the presence of FM and AFM screening channels. The latter give rise to multi-orbital Kondo screening effects. We demonstrated that in order to fully capture this physics, several low-energy ex-

cited states need to be taken into account. From the diagonalization of the magnetic exchange coupling matrix, we introduce the concept of *Kondo orbital*, which allows us to map a real-space localization of the Kondo resonance observed experimentally. The KO concept incorporates the excited state electronic structure through the Schrieffer-Wolff transformation. This allows to overcome the limitations of other quantities frequently used to identify Kondo effects in the dI/dV spatial features, such as frontier orbitals and natural transition orbitals (NTO), which only account for the ground state.

The procedure has been applied to four different open-shell molecules with several unpaired electrons and NRG calculations have confirmed the existence of multi-orbital Kondo effects. In particular, we have been able to reproduce published experimental dI/dV maps and zero-bias spectral features. We anticipate that the presented theoretical framework can be adopted for analysis of the emergence of the Kondo regime in other strongly correlated atomic systems with several unpaired electrons, too.

Appendix A: Schrieffer-Wolff transformation

The effective Kondo interaction for the ionic Anderson Hamiltonian to second order in perturbation theory takes the form

$$\hat{H}_K = \sum_{m_0, m'_0} \int_{-D}^D d\epsilon \int_{-D}^D d\epsilon' T(m_0, \epsilon\alpha i \leftarrow m'_0, \epsilon'\alpha' i') \times \hat{c}_{\epsilon\alpha i}^\dagger |M_0, m_0\rangle \langle M_0, m'_0| \hat{c}_{\epsilon'\alpha' i'}, \quad (\text{A1})$$

where $T(m_0, \epsilon\alpha i \leftarrow m'_0, \epsilon'\alpha' i')$ is the second order scattering amplitude corresponding to virtual processes where an incoming electron with quantum numbers ϵ' (energy), α' (channel) and i' (spin) is scattered off the molecule into a state with quantum numbers ϵ , α and σ , and the molecule spin changes from m'_0 to m_0 . This amplitude can be written as a sum of contributions from

the intermediate excited multiplets,

$$T(m_0, \epsilon\alpha i \leftarrow m'_0, \epsilon'\alpha' i') = \sum_{M_c} T(M_c, N_c, S_c; m_0, \epsilon\alpha i \leftarrow m'_0, \epsilon'\alpha' i'), \quad (\text{A2})$$

where $T(M_c, N_c, S_c; m_0, \epsilon\alpha i \leftarrow m'_0, \epsilon'\alpha' i')$ is the amplitude for processes where the intermediate molecular state belongs to the M_c multiplet, which has occupation and spin quantum numbers N_c, S_c . The Feynman diagrams for such processes are given in Fig. 1.

The amplitude for scattering through an intermediate state with one more electron ($N_c = N_0 + 1$) is

$$T(M_c, N_0 + 1, S_c; m_0, \epsilon\alpha i \leftarrow m'_0, \epsilon'\alpha' i') = -\rho V^2 \frac{\langle M_c | \hat{f}_\alpha^\dagger | M_0 \rangle^* \langle M_c | \hat{f}_{\alpha'}^\dagger | M_0 \rangle}{\epsilon_{M_c} - \epsilon_{M_0}} \times \left(\frac{1}{2}, i; S_0, m_0 | S_c, m_0 + i \right)^* \left(\frac{1}{2}, i'; S_0, m'_0 | S_c, m_0 + i \right), \quad (\text{A3})$$

where we have used the Wigner-Eckart theorem to decompose the excitation matrix elements as

$$\langle M_1, m_1 | \hat{f}_{\alpha i}^\dagger | M_2, m_2 \rangle = \langle M_1 | \hat{f}_\alpha^\dagger | M_2 \rangle \left(\frac{1}{2}, i; S_2, m_2 | S_1, m_1 \right)^*, \quad (\text{A4})$$

where $\langle M_1 | \hat{f}_\alpha^\dagger | M_2 \rangle$ is the reduced matrix element with respect to spin symmetry and the $(\dots; \dots | \dots)$ terms are spin Clebsch-Gordan coefficients, which are given by

$$\left(\frac{1}{2}, \pm \frac{1}{2}; S, m | S + \frac{1}{2}, m \pm \frac{1}{2} \right) = \sqrt{\frac{1}{2} \left(1 \pm \frac{m \pm \frac{1}{2}}{S + \frac{1}{2}} \right)}, \quad (\text{A5})$$

$$\left(\frac{1}{2}, \pm \frac{1}{2}; S, m | S - \frac{1}{2}, m \pm \frac{1}{2} \right) = \mp \sqrt{\frac{1}{2} \left(1 \mp \frac{m \pm \frac{1}{2}}{S + \frac{1}{2}} \right)}. \quad (\text{A6})$$

Applying the previous results to $T(M_c, N_0 + 1, S_0 - \frac{1}{2}; m_0, \epsilon\alpha i \leftarrow m'_0, \epsilon\alpha' i')$, we obtain

$$T(M_c, N_0 + 1, S_0 - \frac{1}{2}; m_0, \epsilon\alpha i \leftarrow m'_0, \epsilon'\alpha' i') = -\rho V^2 \frac{\langle M_c | \hat{f}_\alpha^\dagger | M_0 \rangle^* \langle M_c | \hat{f}_{\alpha'}^\dagger | M_0 \rangle}{\epsilon_{M_c} - \epsilon_{M_0}} \times \begin{cases} -\frac{1}{S_0 + \frac{1}{2}} \frac{1}{2} m_0 + \frac{1}{2} \frac{S_0}{S_0 + 1/2}, & \text{if } i = i' = \frac{1}{2}, m_0 = m'_0, \\ +\frac{1}{S_0 + \frac{1}{2}} \frac{1}{2} m_0 + \frac{1}{2} \frac{S_0}{S_0 + 1/2}, & \text{if } i = i' = -\frac{1}{2}, m_0 = m'_0, \\ -\frac{1}{S_0 + \frac{1}{2}} \frac{1}{2} \sqrt{S_0(S_0 + 1) - m_0(m_0 + 1)}, & \text{if } i = \frac{1}{2}, i' = -\frac{1}{2}, m_0 = m'_0 - 1, \\ -\frac{1}{S_0 + \frac{1}{2}} \frac{1}{2} \sqrt{S_0(S_0 + 1) - m_0(m_0 - 1)}, & \text{if } i = -\frac{1}{2}, i' = \frac{1}{2}, m_0 = m'_0 + 1 \end{cases} \\ = \rho V^2 \frac{\langle M_c | \hat{f}_\alpha^\dagger | M_0 \rangle^* \langle M_c | \hat{f}_{\alpha'}^\dagger | M_0 \rangle}{(\epsilon_{M_c} - \epsilon_{M_0})(S_0 + \frac{1}{2})} \left(\frac{1}{2} \mathbf{S}_{m_0 m'_0} \cdot \boldsymbol{\sigma}_{ii'} + S_0 \delta_{ii'} \delta_{m_0 m'_0} \right). \quad (\text{A7})$$

The diagonal term proportional to $S_0 \delta_{ii'} \delta_{m_0 m'_0}$ gives rise

to a scattering potential that we will ignore from now

on, as its main contribution is to slightly renormalize the magnetic coupling parameters [61]. \mathbf{S} is the matrix representation of the spin (vector) operator, which we obtain together with the Pauli matrices by identifying their components using the expressions

$$\begin{aligned} S_{m_0 m'_0}^z &= m_0 \delta_{m_0, m'_0}, \\ S_{m_0 m'_0}^- &= \sqrt{S_0(S_0 + 1) - m_0(m_0 + 1)} \delta_{m_0, m'_0 - 1}, \\ S_{m_0 m'_0}^+ &= \sqrt{S_0(S_0 + 1) - m_0(m_0 - 1)} \delta_{m_0, m'_0 + 1}. \end{aligned} \quad (\text{A8})$$

$$T(M_c, N_0 - 1, S_0 - \frac{1}{2}; m_0, \epsilon \alpha i \leftarrow m'_0, \epsilon' \alpha' i) = \rho V^2 \frac{\langle M_0 | \hat{f}_\alpha^\dagger | M_c \rangle \langle M_0 | \hat{f}_{\alpha'}^\dagger | M_c \rangle^*}{(\epsilon_{M_c} - \epsilon_{M_0}) S_0} \frac{1}{2} \mathbf{S}_{m_0 m'_0} \cdot \boldsymbol{\sigma}_{ii'}, \quad (\text{A9})$$

$$T(M_c, N_0 + 1, S_0 + \frac{1}{2}; m_0, \epsilon \alpha i \leftarrow m'_0, \epsilon' \alpha' i) = -\rho V^2 \frac{\langle M_c | \hat{f}_\alpha^\dagger | M_0 \rangle^* \langle M_c | \hat{f}_{\alpha'}^\dagger | M_0 \rangle}{(\epsilon_{M_c} - \epsilon_{M_0})(S_0 + \frac{1}{2})} \frac{1}{2} \mathbf{S}_{m_0 m'_0} \cdot \boldsymbol{\sigma}_{ii'}, \quad (\text{A10})$$

$$T(M_c, N_0 - 1, S_0 + \frac{1}{2}; m_0, \epsilon \alpha i \leftarrow m'_0, \epsilon' \alpha' i) = -\rho V^2 \frac{\langle M_0 | \hat{f}_\alpha^\dagger | M_c \rangle \langle M_0 | \hat{f}_{\alpha'}^\dagger | M_c \rangle^*}{(\epsilon_{M_c} - \epsilon_{M_0})(S_0 + 1)} \frac{1}{2} \mathbf{S}_{m_0 m'_0} \cdot \boldsymbol{\sigma}_{ii'}. \quad (\text{A11})$$

Substituting Eqs. A7, A9, A10 and A11 in Eq. A1, we obtain the Kondo Hamiltonian

$$\hat{H}_K = \frac{J_{\alpha\alpha'}}{2} \sum_{i,i'} \sum_{\alpha,\alpha'} (\hat{\mathbf{S}} \cdot \boldsymbol{\sigma}_{ii'}) \hat{\psi}_{\alpha i}^\dagger \hat{\psi}_{\alpha' i'}, \quad (\text{A12})$$

where $J_{\alpha\alpha'}$ is given by Eqs. 7 and 8, $\hat{\mathbf{S}} = \sum_{m_0 m'_0} \mathbf{S}_{m_0 m'_0} |M_0 m_0\rangle \langle M_0 m'_0|$ is the impurity spin operator, and $\hat{\mathbf{s}}_{\alpha\alpha'}$ is the local spin density operator of the conduction electrons [31],

$$\hat{\mathbf{s}}_{\alpha\alpha'} = \sum_{ii'} \frac{1}{2} \hat{\psi}_{\alpha i}^\dagger \boldsymbol{\sigma}_{ii'} \hat{\psi}_{\alpha' i'}, \quad (\text{A13})$$

where the $\hat{\psi}_{\alpha i}^{(\dagger)}$ operators are defined as $\hat{\psi}_{\alpha i} = \int d\epsilon \rho^{\frac{1}{2}} \hat{c}_{\epsilon\alpha i}$ and fulfill the commutation relation $\{\hat{\psi}_{\alpha i}^\dagger, \hat{\psi}_{\alpha' i'}\} = \delta_{\alpha\alpha'} \delta_{ii'}$.

Throughout the calculation, we have ignored the renormalization of the excitation energies. Although its effect is usually small for systems close to particle-hole symmetry, in particle-hole asymmetric cases it can result in the renormalization of coupling constants, in driving the system close to the mixed-valence regime, and even in changes in the ground state as the temperature is lowered [61]. In principle, this could be relevant for the **ETRI** and **A5T** molecules (Sections IV C and IV D). For those systems, we rely on the NRG calculations to verify that the system does indeed exhibit the zero-bias peaks characteristic of the Kondo regime and that the larger peak widths correspond to the largest coupling constants.

Appendix B: Scaling equations for the coupling constants

The scaling equations for the coupling constants $J_{\alpha\alpha'}$ and j_a are obtained using the poor man's scaling method

Following the same procedure for the remaining N_c, S_c combinations, we obtain the following contributions from second-order scattering to the magnetic coupling:

[42] to the Kondo interaction derived in Section B. Following a procedure analogous to the Schrieffer-Wolff transformation in Appendix A, we sum over the second-order processes depicted in Fig. 12 to eliminate electronic degrees of freedom lying in the energy range $|\epsilon| \in [D - |\delta D|, D]$. By doing so, we obtain the differential scaling of the Kondo interaction,

$$\begin{aligned} \delta \hat{\mathcal{H}}_K &= \sum_{m_0, m'_0} \int_{-D}^D d\epsilon \int_{-D}^D d\epsilon' \delta T(m_0, \epsilon \alpha i \leftarrow m'_0, \epsilon' \alpha' i) \\ &\quad \times \hat{c}_{\epsilon\alpha i}^\dagger |M_0, m_0\rangle \langle M_0, m'_0| \hat{c}_{\epsilon' \alpha' i'}, \end{aligned} \quad (\text{B1})$$

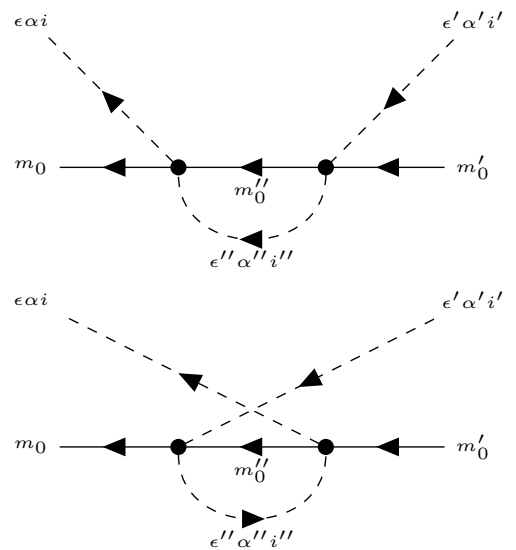


FIG. 12. Feynman diagrams for virtual processes with an intermediate electron (left) and hole (left).

where $\delta T(m_0, \epsilon \alpha i \leftarrow m'_0, \epsilon' \alpha' i')$ is the sum over second order scattering amplitudes involving the creation of an intermediate particle (p) with or hole (h) with energy

$$|\epsilon| \in [D - \delta D, D]:$$

$$\begin{aligned} \delta T(m_0, \epsilon \alpha i \leftarrow m'_0, \epsilon' \alpha' i') &= \delta T_p(m_0, \epsilon \alpha i \leftarrow m'_0, \epsilon' \alpha' i') \\ &+ \delta T_h(m_0, \epsilon \alpha i \leftarrow m'_0, \epsilon' \alpha' i'). \end{aligned} \quad (\text{B2})$$

To compute the scattering amplitudes, we generalize the equations in [62] to include many channels. For the contribution from processes with an intermediate particle, we obtain

$$\begin{aligned} \delta T_p(m_0, \epsilon \alpha i \leftarrow m'_0, \epsilon' \alpha' i') &= \sum_{\alpha'', m''_0} \frac{1}{2} \rho J_{\alpha \alpha''} (\mathbf{S}_{m_0 m''_0} \cdot \boldsymbol{\sigma}_{ii''}) \frac{\delta D}{(-D)} \frac{1}{2} \rho J_{\alpha'' \alpha'} (\mathbf{S}_{m''_0 m'_0} \cdot \boldsymbol{\sigma}_{i'' i'}) \\ &= -\frac{1}{4} \rho^2 [J^2]_{\alpha \alpha'} \frac{\delta D}{D} \sum_{a,b} [S^a S^b]_{m_0 m'_0} [\sigma^a \sigma^b]_{ii'} \end{aligned} \quad (\text{B3})$$

for the scattering through intermediate states with an excited electron, where $\rho \delta D$ is the number of particle states in the $[D - \delta D, D]$ energy range and S^a and σ^a are the a components of \mathbf{S} and $\boldsymbol{\sigma}$, respectively. For the scattering through an intermediate state with the incoming electron plus an electron-hole pair, we have

$$\begin{aligned} \delta T_h(m_0, \epsilon \alpha i \leftarrow m'_0, \epsilon' \alpha' i') &= \sum_{\alpha'', m''_0} -\frac{1}{2} \rho J_{\alpha \alpha''} (\mathbf{S}_{m_0 m''_0} \cdot \boldsymbol{\sigma}_{i'' i'}) \frac{\delta D}{(-D)} \frac{1}{2} \rho J_{\alpha \alpha'} (\mathbf{S}_{m''_0 m'_0} \cdot \boldsymbol{\sigma}_{ii'}) \\ &= \frac{1}{4} \rho^2 \frac{\delta D}{D} [J^2]_{\alpha \alpha'} \sum_{a,b} [S^a S^b]_{m_0 m'_0} [\sigma^b \sigma^a]_{ii'}. \end{aligned} \quad (\text{B4})$$

To obtain the total amplitude, we sum the particle and hole terms and apply the commutation relations of the spin and Pauli matrices to arrive at

$$\delta T(m_0, \epsilon \alpha i \leftarrow m'_0, \epsilon' \alpha' i') = -\frac{1}{2} \rho^2 [J^2]_{\alpha \alpha'} \frac{\delta D}{D} \mathbf{S}_{m_0 m'_0} \cdot \boldsymbol{\sigma}_{ii'}. \quad (\text{B5})$$

Introducing this in Eq. B1, we get

$$\begin{aligned} \delta \hat{H}_K &= - \sum_{m_0, m'_0} \sum_{i, i'} \sum_{\alpha, \alpha'} \int_{-D}^D d\epsilon \int_{-D}^D d\epsilon' \frac{1}{2} \rho^2 [J^2]_{\alpha \alpha'} \frac{\delta D}{D} \\ &\times (\mathbf{S}_{m_0 m'_0} \cdot \boldsymbol{\sigma}_{ii'}) \hat{c}_{\epsilon \alpha i}^\dagger |M_0, m_0\rangle \langle M_0, m'_0| \hat{c}_{\epsilon' \alpha' i'} \\ &= - \sum_{i, i'} \sum_{\alpha, \alpha'} \frac{1}{2} \rho [J^2]_{\alpha \alpha'} \frac{\delta D}{D} (\hat{\mathbf{S}} \cdot \boldsymbol{\sigma}_{ii'}) \hat{\psi}_{\alpha i}^\dagger \hat{\psi}_{\alpha' i'}. \end{aligned} \quad (\text{B6})$$

Isolating the coupling constant, we find

$$\delta J_{\alpha \alpha'} = \rho [J^2]_{\alpha \alpha'} \frac{|\delta D|}{D}. \quad (\text{B7})$$

In the diagonal channel basis, this reduces to the simple expression

$$\delta j_a = \rho j_a^2 \frac{|\delta D|}{D}, \quad (\text{B8})$$

Therefore, as the energy scale is lowered, the magnitude $|j_a|$ of the coupling will grow in antiferromagnetically

coupled channels ($j_a > 0$) decrease in the ferromagnetically coupled channels ($j_a < 0$).

Appendix C: Natural transition orbitals and Kondo orbitals

To prove that $T = T^\dagger$, we introduce the resolution of the identity $\hat{I} = \sum_{M, m} |Mm\rangle \langle Mm|$ in Eq. 14 and we apply the Wigner-Eckart theorem,

$$\begin{aligned} T_{\alpha \alpha'} &= \langle M_0, m_0 - 1 | \hat{f}_{\alpha \downarrow}^\dagger \hat{I} \hat{f}_{\alpha' \uparrow} | M_0, m_0 \rangle \\ &= \sum_{M, m} \langle M_0 | \hat{f}_{\alpha \downarrow}^\dagger | M \rangle \left(\frac{1}{2}, -\frac{1}{2}; S, m | S_0, m_0 - 1\right)^* \\ &\quad \times \langle M_0 | \hat{f}_{\alpha' \uparrow} | M \rangle^* \left(\frac{1}{2}, \frac{1}{2}; S, m | S_0, m_0\right). \end{aligned} \quad (\text{C1})$$

Since we can choose the molecular states to be real, it follows that the reduced matrix elements can also be chosen as real and therefore $T_{\alpha \alpha'}$ is invariant under swapping the indices α and α' .

To compare NTOs and the KOs analytically, we begin by rewriting the matrix elements of T as

$$\begin{aligned} 2 \cdot T_{\alpha \alpha'} &= \langle M_0, m_0 - 1 | \hat{f}_{\alpha \downarrow}^\dagger \hat{I} \hat{f}_{\alpha' \uparrow} | M_0, m_0 \rangle \\ &\quad - \langle M_0, m_0 - 1 | \hat{f}_{\alpha' \downarrow} \hat{I} \hat{f}_{\alpha \uparrow}^\dagger | M_0, m_0 \rangle, \end{aligned} \quad (\text{C2})$$

where we have used the commutation relation $\{\hat{f}_{\alpha \downarrow}^\dagger, \hat{f}_{\alpha' \uparrow}\} = 0$. Following the same matrix element expansion as in Appendix A, we arrive at results similar to Eqs. A7, A9, A10 and A11,

$$\langle M_0, m_0 - 1 | \hat{f}_{\alpha\downarrow}^\dagger \hat{I} \hat{f}_{\alpha'\uparrow} | M_0, m_0 \rangle = \frac{1}{2} S_{m_0-1, m_0}^- \sum_{M_c} \frac{\langle M_0 | \hat{f}_{\alpha}^\dagger | M_c \rangle \langle M_c | \hat{f}_{\alpha'} | M_0 \rangle}{F(N_0 - 1, S_c, S_0)}, \quad (\text{C3})$$

$$\langle M_0, m_0 - 1 | \hat{f}_{\alpha'\uparrow} \hat{I} \hat{f}_{\alpha\downarrow}^\dagger | M_0, m_0 \rangle = -\frac{1}{2} S_{m_0-1, m_0}^- \sum_{M_c} \frac{\langle M_0 | \hat{f}_{\alpha}^\dagger | M_c \rangle \langle M_c | \hat{f}_{\alpha'} | M_0 \rangle}{F(N_0 + 1, S_c, S_0)}, \quad (\text{C4})$$

where

$$F(N_c, S_c, S_0) = \begin{cases} (S_0 + \frac{1}{2}), & \text{if } N_c = N_0 + 1, S_c = S_0 - \frac{1}{2}, \\ S_0, & \text{if } N_c = N_0 - 1, S_c = S_0 - \frac{1}{2}, \\ -(S_0 + \frac{1}{2}), & \text{if } N_c = N_0 + 1, S_c = S_0 + \frac{1}{2}, \\ -(S_0 + 1), & \text{if } N_c = N_0 - 1, S_c = S_0 + \frac{1}{2} \end{cases} \quad (\text{C5})$$

is the same factor appearing in Eq. 8. Therefore, the matrix elements $T_{\alpha\alpha'}$ can be written compactly as in Eq. 15.

Appendix D: Electronic structure of the molecules

Here we describe the many-body wave function of the ground and excited states obtained from CASCI calculations for neutral (N) and charged ($N \pm 1$) states for all molecules presented in this manuscript. In the case of neutral molecules we employed CAS(12,12), but most of the many-body character in the Slater-determinants arises in the orbitals around the Fermi level. Therefore, to make the many-body representation of the wave-functions we use only six electrons.

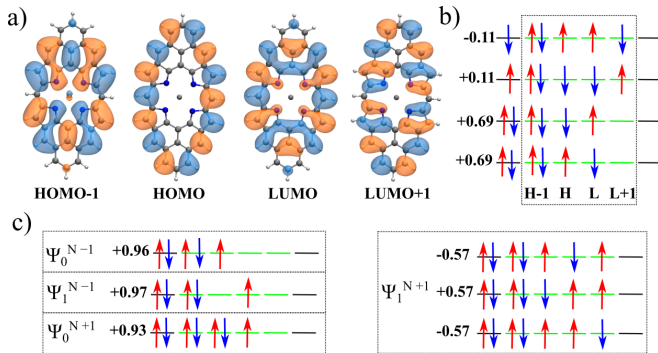


FIG. 13. a) The four main DFT orbitals employed in the active space calculation for the **PorA₂** molecule. b) Major Slater determinants for the ground states **PorA₂**. The dashed box contains the four frontier orbitals: HOMO-1, HOMO, LUMO, and LUMO+1. The values are the coefficients of those determinants in the orbital wave function. c) Major Slater determinants for N-1 and N+1 charge states for ground and first multiplet.

State	N	N-1	N+1
Ground	0.0000(1)	7.9298(0.5)	2.0303(0.5)
1 st excited	0.0527(0)	8.2659(0.5)	2.3651(1.5)
2 nd excited	1.1738(1)	9.0140(0.5)	2.5542(0.5)
3 rd excited	1.6342(0)	9.2818(1.5)	2.7697(0.5)

TABLE I. Calculated energies and spin (in parentheses) of the ground state and lowest excited states for the neutral (N) and charged ($N \pm 1$) charge states obtained from CASCI calculations of the gas-phase **PorA₂** molecule. The energies (in eV) include the chemical potential $\mu = 3$ eV and are aligned to the ground state of the neutral molecule, which is set to zero.

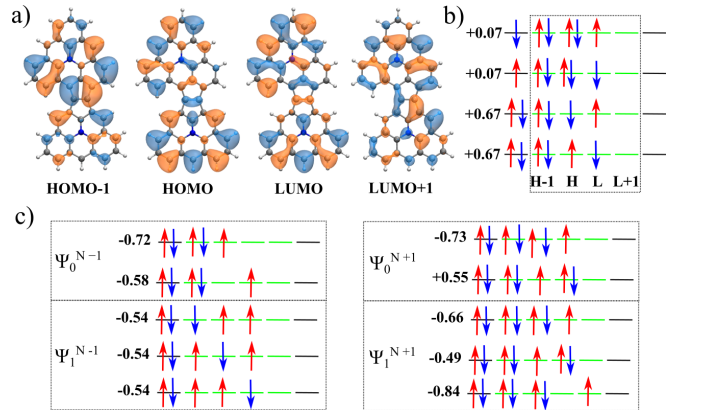


FIG. 14. a) The four main DFT orbitals employed in the active space calculation for the **4²⁺** molecule. b) Major Slater determinants for the ground states **4²⁺** molecule. The dashed box contains the four frontier orbitals: HOMO-1, HOMO, LUMO, and LUMO+1. The values are the coefficients of those determinants in the orbital wave function. c) Major Slater determinants for N-1 and N+1 charge states for ground and first multiplet.

State	N	N-1	N+1
Ground	0.0000(1)	12.0506(0.5)	1.8190(0.5)
1 st excited	0.0009(0)	12.5610(1.5)	2.4848(0.5)
2 nd excited	1.6143(0)	12.7091(0.5)	2.8623(1.5)
3 rd excited	1.8229(1)	12.9194(0.5)	3.0735(0.5)

TABLE II. Same as Table I for the **4^{'''}** molecule with the chemical potential $\mu = 5$ eV.

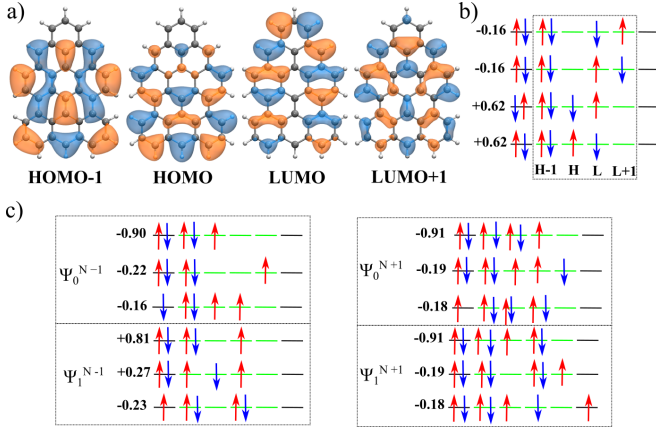


FIG. 15. a) The four main DFT orbitals employed in the active space calculation for the **ETRI** molecule. b) Major Slater determinants for the ground states **ETRI** molecule. The dashed box contains the four frontier orbitals: HOMO-1, HOMO, LUMO, and LUMO+1. The values are the coefficients of those determinants in the orbital wave function. c) Major Slater determinants for N-1 and N+1 charge states for ground and first multiplet.

State	N	N-1	N+1
Ground	0.0000(1)	8.7642(0.5)	3.8533(0.5)
1 st excited	0.3618(0)	8.9630(0.5)	4.0815(0.5)
2 nd excited	1.2966(0)	10.6777(1.5)	5.6539(1.5)
3 rd excited	2.1004(0)	11.1707(1.5)	6.1963(0.5)

TABLE III. Same as Table I for the **ETRI** molecule with the chemical potential $\mu = 4$ eV

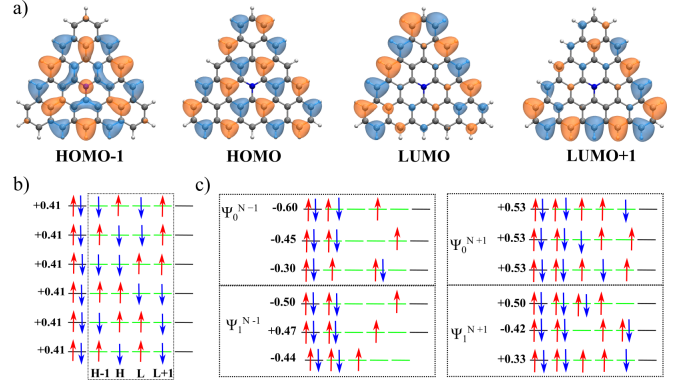


FIG. 16. a) The four main DFT orbitals employed in the active space calculation for the **A5T** molecule. b) Major Slater determinants for the ground states **A5T** molecule. The dashed box contains the four frontier orbitals: HOMO-1, HOMO, LUMO, and LUMO+1. The values are the coefficients of those determinants in the orbital wave function. c) Major Slater determinants for N-1 and N+1 charge states for ground and first multiplet.

State	N	N-1	N+1
Ground	0.0000(2)	12.0759(0.5)	0.4809(1.5)
1 st excited	0.5491(1)	12.1114(0.5)	0.9573(0.5)
2 nd excited	0.5701(1)	12.2326(0.5)	0.9675(0.5)
3 rd excited	0.8931(0)	12.2585(1.5)	1.4241(1.5)

TABLE IV. Same as Table I for the **A5T** molecule with the chemical potential $\mu = 4.3$ eV.

Appendix E: Reduced Lehmann amplitudes

The reduced matrix elements $\langle M_c | \hat{f}_\alpha^{(\dagger)} | M_0 \rangle$ appearing in the Schrieffer-Wolf transformation are shown below for the four studied molecules.

	M_c	M_{0-}	M_{1-}	M_{0+}	M_{1+}
α	1	0.00	0.00	0.00	-0.09
	2	0.00	0.00	0.00	0.00
	3	0.00	-0.96	-1.23	0.00
	4	-0.97	0.00	0.00	0.00
	5	0.00	0.00	0.00	0.96
	6	0.00	0.04	-0.20	0.00

TABLE V. Reduced matrix elements $\langle M_c | \hat{f}_\alpha^{(\dagger)} | M_0 \rangle$ for positively (+) and negatively (-) charged excited multiplets M_c for the **PorA₂** molecule.

M_c	M_{0-}	M_{1-}	M_{0+}	M_{1+}	
α	1	-0.03	0.06	-0.03	0.06
	2	-0.02	0.77	0.01	0.00
	3	0.42	0.00	0.53	-0.35
	4	-0.50	-0.01	0.39	0.47
	5	0.03	0.04	-0.04	0.11
	6	-0.01	0.01	0.07	-0.07

TABLE VI. Same as Table V for the $4''^+$ molecule.

M_c	M_{0-}	M_{1-}	M_{0+}	M_{1+}	
α	1	0.16	0.00	0.00	-0.21
	2	0.00	0.19	-0.11	0.00
	3	0.00	-0.89	1.14	0.00
	4	-0.93	0.00	0.00	1.11
	5	0.00	-0.21	0.22	0.00
	6	0.00	-0.03	0.01	0.00

TABLE VII. Same as Table V for the **ETRI** molecule.

M_c	M_{0-}	M_{1-}	M_{0+}	M_{1+}	
α	1	-0.02	-0.04	0.00	0.00
	2	0.00	-0.04	-1.03	0.00
	3	0.37	-0.03	0.00	1.11
	4	-0.03	-0.96	0.00	0.00
	5	-0.89	0.02	0.00	-0.02
	6	0.00	0.00	0.36	0.00

TABLE VIII. Same as Table V for the **A5T** molecule.

ACKNOWLEDGMENTS

A.C.-F., A.E. and M.B.-R. acknowledge grants No. IT-1527-22, funded by the Department of Education, Universities and Research of the Basque Government, and PID2022-137685NB-I00, funded by MCIN/AEI 10.13039/501100011033/ and by “ERDF A way of making Europe”. A.C.-F. acknowledges grant No. PRE2020-092046 funded by the Spanish MCIN. D.S., M.K. and P.J. acknowledge financial support from the Czech-NanoLab Research Infrastructure supported by MEYS CR (LM2023051) and the GACR project no. 23-05486S. We acknowledge fruitful discussion with L. Veis and F. Flores.

-
- [1] A. C. Hewson, *The Kondo Problem to Heavy Fermions*, Cambridge Studies in Magnetism (Cambridge University Press, 1993).
- [2] J. Kondo, Resistance minimum in dilute magnetic alloys, *Progress of theoretical physics* **32**, 37 (1964).
- [3] W. de Haas, J. de Boer, and G. van den Berg, The electrical resistance of gold, copper and lead at low temperatures, *Physica* **1**, 1115–1124 (1934).
- [4] *Nature Physics* **10**, 329–329 (2014).
- [5] V. Madhavan, W. Chen, T. Jamneala, M. F. Crommie, and N. S. Wingreen, Tunneling into a single magnetic atom: Spectroscopic evidence of the Kondo resonance, *Science* **280**, 567 (1998).
- [6] J. Li, W.-D. Schneider, R. Berndt, and B. Delley, Kondo scattering observed at a single magnetic impurity, *Phys. Rev. Lett.* **80**, 2893 (1998).
- [7] N. Knorr, M. A. Schneider, L. Diekhöner, P. Wahl, and K. Kern, Kondo effect of single Co adatoms on Cu surfaces, *Phys. Rev. Lett.* **88**, 096804 (2002).
- [8] A. F. Otte, M. Ternes, K. von Bergmann, S. Loth, H. Brune, C. P. Lutz, C. F. Hirjibehedin, and A. J. Heinrich, The role of magnetic anisotropy in the Kondo effect, *Nature Physics* **4**, 847 (2008).
- [9] T. Esat, T. Deilmann, B. Lechtenberg, C. Wagner, P. Krüger, R. Temirov, F. B. Anders, M. Rohlfing, and F. S. Tautz, Transferring spin into an extended π orbital of a large molecule, *Phys. Rev. B* **91**, 144415 (2015).
- [10] G. D. Scott and D. Natelson, Kondo resonances in molecular devices, *ACS Nano* **4**, 3560 (2010).
- [11] T. Komeda, H. Isshiki, J. Liu, Y.-F. Zhang, N. Lorente, K. Katoh, B. K. Breedlove, and M. Yamashita, Observation and electric current control of a local spin in a single-molecule magnet, *Nature Communications* **2**, 217 (2011).
- [12] E. Minamitani, N. Tsukahara, D. Matsunaka, Y. Kim, N. Takagi, and M. Kawai, Symmetry-driven novel Kondo effect in a molecule, *Phys. Rev. Lett.* **109**, 086602 (2012).
- [13] R. Hiraoka, E. Minamitani, R. Arafune, N. Tsukahara, S. Watanabe, M. Kawai, and N. Takagi, Single-molecule quantum dot as a Kondo simulator, *Nature Communications* **8**, 16012 (2017).
- [14] R. Žitko, G. G. Blesio, L. O. Manuel, and A. A. Aligia, Iron phthalocyanine on au(111) is a “non-Landau” Fermi liquid, *Nature Communications* **12**, 6027 (2021).
- [15] I. Fernández-Torrente, K. J. Franke, and J. I. Pascual, Vibrational Kondo effect in pure organic charge-transfer assemblies, *Phys. Rev. Lett.* **101**, 217203 (2008).
- [16] T. Choi, S. Bedwani, A. Rochefort, C.-Y. Chen, A. J. Epstein, and J. A. Gupta, A single molecule Kondo switch: Multistability of tetracyanoethylene on cu(111), *Nano Letters* **10**, 4175 (2010).

- [17] U. G. E. Perera, H. J. Kulik, V. Iancu, L. G. G. V. Dias da Silva, S. E. Ulloa, N. Marzari, and S.-W. Hla, Spatially extended Kondo state in magnetic molecules induced by interfacial charge transfer, *Phys. Rev. Lett.* **105**, 106601 (2010).
- [18] R. Requist, S. Modesti, P. P. Baruselli, A. Smogunov, M. Fabrizio, and E. Tosatti, Kondo conductance across the smallest spin 1/2 radical molecule, *Proceedings of the National Academy of Sciences* **111**, 69 (2014).
- [19] E. Minamitani, Y.-S. Fu, Q.-K. Xue, Y. Kim, and S. Watanabe, Spatially extended underscreened Kondo state from collective molecular spin, *Phys. Rev. B* **92**, 075144 (2015).
- [20] L. L. Patera, S. Sokolov, J. Z. Low, L. M. Campos, L. Venkataraman, and J. Repp, Resolving the unpaired-electron orbital distribution in a stable organic radical by Kondo resonance mapping, *Angewandte Chemie International Edition* **58**, 11063 (2019).
- [21] H. Koshida, H. Okuyama, S. Hatta, T. Aruga, and E. Minamitani, Effect of local geometry on magnetic property of nitric oxide on Au(110)-(1 × 2), *Phys. Rev. B* **103**, 155412 (2021).
- [22] S. Lu, H. Nam, P. Xiao, M. Liu, Y. Guo, Y. Bai, Z. Cheng, J. Deng, Y. Li, H. Zhou, G. Henkelman, G. A. Fiete, H.-J. Gao, A. H. MacDonald, C. Zhang, and C.-K. Shih, PTCDA molecular monolayer on Pb thin films: An unusual π -electron Kondo system and its interplay with a quantum-confined superconductor, *Phys. Rev. Lett.* **127**, 186805 (2021).
- [23] J. Li, S. Sanz, M. Corso, D. J. Choi, D. Peña, T. Frederiksen, and J. I. Pascual, Single spin localization and manipulation in graphene open-shell nanostructures, *Nature Communications* **10** (2019).
- [24] J. Li, S. Sanz, J. Castro-Esteban, M. Vilas-Varela, N. Friedrich, T. Frederiksen, D. Peña, and J. I. Pascual, Uncovering the triplet ground state of triangular graphene nanoflakes engineered with atomic precision on a metal surface, *Phys. Rev. Lett.* **124**, 177201 (2020).
- [25] S. Mishra, D. Beyer, K. Eimre, S. Kezilebieke, R. Berger, O. Gröning, C. A. Pignedoli, K. Müllen, P. Liljeroth, P. Ruffieux, X. Feng, and R. Fasel, Topological frustration induces unconventional magnetism in a nanographene, *Nature Nanotechnology* **15**, 22 (2020).
- [26] D. Jacob, R. Ortiz, and J. Fernández-Rossier, Renormalization of spin excitations and Kondo effect in open-shell nanographenes, *Phys. Rev. B* **104**, 075404 (2021).
- [27] E. Turco, A. Bernhardt, N. Krane, L. Valenta, R. Fasel, M. Juríček, and P. Ruffieux, Observation of the magnetic ground state of the two smallest triangular nanographenes, *JACS Au* **3**, 1358 (2023).
- [28] Nozières, Ph. and Blandin, A., Kondo effect in real metals, *J. Phys. France* **41**, 193 (1980).
- [29] N. Roch, S. Florens, T. A. Costi, W. Wernsdorfer, and F. Balestro, Observation of the underscreened Kondo effect in a molecular transistor, *Phys. Rev. Lett.* **103**, 197202 (2009).
- [30] J. J. Parks, A. R. Champagne, T. A. Costi, W. W. Shum, A. N. Pasupathy, E. Neuscamman, S. Flores-Torres, P. S. Cornaglia, A. A. Aligia, C. A. Balseiro, G. K.-L. Chan, H. D. A. na, and D. C. Ralph, Mechanical control of spin states in spin-1 molecules and the underscreened Kondo effect, *Science* **328**, 1370 (2010).
- [31] M. Pustilnik and L. I. Glazman, Kondo effect in real quantum dots, *Physical Review Letters* **87**, 216601 (2001).
- [32] A. Mitchell, K. Pedersen, P. Hedegård, and J. Paaske, Kondo blockade due to quantum interference in single-molecule junctions, *Nature Communications* **8**, 15210 (2017).
- [33] J. Girovsky, J. Nowakowski, M. E. Ali, M. Baljovic, H. R. Rossmann, T. Nijs, E. A. Aebly, S. Nowakowska, D. Siewert, G. Srivastava, C. Wäckerlin, J. Dreiser, S. Decurtins, S.-X. Liu, P. M. Oppeneer, T. A. Jung, and N. Ballav, Long-range ferrimagnetic order in a two-dimensional supramolecular Kondo lattice, *Nature Communications* **8**, 15388 (2017).
- [34] K. Biswas, M. Urbani, A. Sánchez-Grande, D. Soler-Polo, K. Lauwaet, A. Matěj, P. Mutombo, L. Veis, J. Brabec, K. Pernal, J. M. Gallego, R. Miranda, D. ěcija, P. Jelínek, T. Torres, and J. I. Urgel, Interplay between π -conjugation and exchange magnetism in one-dimensional porphyrinoid polymers, *Journal of the American Chemical Society* **144**, 12725 (2022).
- [35] Q. Sun, L. M. Mateo, R. Robles, P. Ruffieux, N. Lorente, G. Bottari, T. Torres, and R. Fasel, Inducing open-shell character in porphyrins through surface-assisted phenalenyl π -extension, *Journal of the American Chemical Society* **142**, 18109 (2020).
- [36] B. O. Roos, P. R. Taylor, and P. E. Sigbahn, A complete active space SCF method (CASSCF) using a density matrix formulated super-CI approach, *Chemical Physics* **48**, 157 (1980).
- [37] H. R. Krishna-murthy, J. W. Wilkins, and K. G. Wilson, Renormalization-group approach to the Anderson model of dilute magnetic alloys. I. Static properties for the symmetric case, *Physical Review B* **21**, 1003 (1980).
- [38] J. P. Calupitan, A. Berdonces-Layunta, F. Aguilar-Galindo, M. Vilas-Varela, D. Peña, D. Casanova, M. Corso, D. G. de Oteyza, and T. Wang, Emergence of π -magnetism in fused Aza-Triangulenes: Symmetry and charge transfer effects, *Nano Letters* **23**, 9832 (2023).
- [39] M. Vilas-Varela, F. Romero-Lara, A. Vegliante, J. P. Calupitan, A. Martínez, L. Meyer, U. Uriarte-Amiano, N. Friedrich, D. Wang, F. Schulz, N. E. Koval, M. E. Sandoval-Salinas, D. Casanova, M. Corso, E. Artacho, D. Peña, and J. I. Pascual, On-surface synthesis and characterization of a high-spin Aza-[5]-Triangulene, *Angewandte Chemie International Edition* **62**, e202307884 (2023).
- [40] A. A. Ovchinnikov, Multiplicity of the ground state of large alternant organic molecules with conjugated bonds, *Theoretica chimica acta* **47**, 297 (1978).
- [41] M. Ternes, Spin excitations and correlations in scanning tunneling spectroscopy, *New Journal of Physics* **17**, 063016 (2015).
- [42] P. W. Anderson, A poor man's derivation of scaling laws for the Kondo problem, *J. Phys. C: Solid St. Phys* **3** (1970).
- [43] L. Hirst, Theory of the coupling between conduction electrons and moments of 3d and 4f ions in metals, *Advances in Physics* **27**, 231 (1978).
- [44] J. R. Schrieffer and P. A. Wolff, Relation between the anderson and kondo hamiltonians, *J. Kondo, Progr. Theoret. Phys. (Kyoto)* **14**, 61 (1966).
- [45] F. Flores and E. C. Goldberg, Ionic Hamiltonians for transition metal atoms: effective exchange coupling and Kondo temperature, *Journal of Physics: Condensed Matter* **29**, 055602 (2016).

- [46] S. Sen and A. K. Mitchell, Many-body quantum interference route to the two-channel kondo effect: Inverse design for molecular junctions and quantum dot devices, *Phys. Rev. Lett.* **133**, 076501 (2024).
- [47] A. Calvo-Fernández, M. Blanco-Rey, and A. Eiguren, The PointGroupNRG code for numerical renormalization group calculations with discrete point-group symmetries, *Computer Physics Communications* **296**, 109032 (2024).
- [48] A. Calvo-Fernández, PointGroupNRG, <https://github.com/aitorcf/PointGroupNRG> (2024).
- [49] M. Gruber, A. Weismann, and R. Berndt, The Kondo resonance line shape in scanning tunnelling spectroscopy: instrumental aspects, *Journal of Physics: Condensed Matter* **30**, 424001 (2018).
- [50] T. A. Costi and A. C. Hewson, Resistivity cross-over for the non-degenerate Anderson model, *Philosophical Magazine B* **65**, 1165 (1992).
- [51] V. L. Campo and L. N. Oliveira, Alternative discretization in the numerical renormalization-group method, *Phys. Rev. B* **72**, 104432 (2005).
- [52] J. P. Perdew, M. Ernzerhof, and K. Burke, Rationale for mixing exact exchange with density functional approximations, *The Journal of Chemical Physics* **105**, 9982 (1996).
- [53] V. Blum, R. Gehrke, F. Hanke, P. Havu, V. Havu, X. Ren, K. Reuter, and M. Scheffler, Ab initio molecular simulations with numeric atom-centered orbitals, *Computer Physics Communications* **180**, 2175 (2009).
- [54] J. P. Perdew, K. Burke, and M. Ernzerhof, Generalized gradient approximation made simple, *Phys. Rev. Lett.* **77**, 3865 (1996).
- [55] P.-O. Löwdin, Quantum theory of many-particle systems. I. Physical interpretations by means of density matrices, natural spin-orbitals, and convergence problems in the method of configurational interaction, *Phys. Rev.* **97**, 1474 (1955).
- [56] F. Neese, The ORCA program system, *WIREs Computational Molecular Science* **2**, 73 (2012).
- [57] F. Neese, Software update: the ORCA program system, version 4.0, *WIREs Computational Molecular Science* **8** (2018).
- [58] O. Krejčí, P. Hapala, M. Ondráček, and P. Jelínek, Principles and simulations of high-resolution STM imaging with a flexible tip apex, *Physical Review B* **95** (2017).
- [59] H. O. Froyen, Shape of the Kondo resonance, *Phys. Rev. B* **45**, 1096 (1992).
- [60] J. Li, S. Sanz, J. Castro-Esteban, M. Vilas-Varela, N. Friedrich, T. Frederiksen, D. Peña, and J. I. Pascual, Uncovering the triplet ground state of triangular graphene nanoflakes engineered with atomic precision on a metal surface, *Phys. Rev. Lett.* **124**, 177201 (2020).
- [61] H. R. Krishna-murthy, J. W. Wilkins, and K. G. Wilson, Renormalization-group approach to the Anderson model of dilute magnetic alloys. II. Static properties for the asymmetric case, *Phys. Rev. B* **21**, 1044 (1980).
- [62] P. Coleman, *Introduction to Many-Body Physics* (Cambridge University Press, 2015).